Terahertz electronic and optoelectronic components and systems

Uncooled bolometer-type Terahertz focal plane array and camera for real-time imaging

Détecteur matriciel de type bolométrique à température ambiante et camera vidéo pour l'imagerie térahertz

Naoki Oda

NEC Corporation, Guidance and Electro-Optics Division, 1-10, Nisshin-Cho, Fuchu, Tokyo 183-8501, Japan

ABSTRACT

Real-time Terahertz (THz) imaging technologies which make use of uncooled bolometer-type infrared focal plane arrays (FPAs) and quantum cascade lasers (QCLs) will be reviewed. A description of how THz focal plane array and THz imagers have been developed on the basis of infrared technologies, especially the improvement in both THz sensitivity of bolometer-type FPA and THz transmittance of materials for lens and vacuum package window will be given. Characteristics of 320×240 THz-FPA, such as relation of noise equivalent power (NEP) to wavelength and real-time THz imageries will be presented. One of the imageries indicates that THz technology is promising for label-free detection of reaction of small molecules with proteins.

© 2010 Académie des sciences. Published by Elsevier Masson SAS. All rights reserved.

RÉSUMÉ

L'auteur présente une revue des techniques pour l'imagerie térahertz en temps réel, basées sur des détecteurs matriciels formés de bolomètres non refroidis placés dans le plan focal d'une caméra, et éclairés par des lasers à cascade quantique. Il décrit le développement technologique de ces détecteurs et des imageurs THz, qui a démarré à partir de systèmes conçus initialement pour l'imagerie infrarouge. En particulier, l'effort technologique a porté sur l'augmentation de la sensibilité des détecteurs dans le domaine THz, et sur l'emploi de matériaux très transparents pour fabriquer les optiques et fenêtres du système. Les caractéristiques et performances du dispositif actuel conçu et fabriqué par l'auteur, qui comprend 320×240 pixels, sont données, comme la puissance de bruit équivalente en fonction de la longueur d'onde des signaux térahertz. Des exemples d'images térahertz enregistrées avec cet imageur sont présentés. Ainsi, il est possible de détecter la réaction chimique de petites molécules avec des protéines, sans requérir à des marqueurs, ce qui est très prometteur en termes d'applications pour la biologie.

© 2010 Académie des sciences. Published by Elsevier Masson SAS. All rights reserved.

1. Introduction

Terahertz (THz) frequency range radiation, 0.1–10 THz (wavelength range of 30 µm–3 mm), has shown promise for security and biochemical imaging applications because of spectral features which allow the detection of illicit drugs in

mail screening [1], explosives [2] and probably biological warfare agents [3]. THz imaging technology is also promising for situational awareness at a disaster site, where a lot of smoke and dust particles exist, because the scattering loss at THz is much smaller than that at visible and infrared frequencies. For these applications, real-time (~30 frames per second) imaging technology is highly desirable, which requires two-dimensional array sensor, in other words, focal plane array (FPA) and a high transmission THz lens.

The author first summarizes previous works on real-time THz imaging which made use of uncooled bolometer-type infrared focal plane arrays (IRFPAs) and quantum cascade lasers (QCLs). Second, he describes thermal isolation structure of THz-FPA, method of improvement in THz sensitivity and the search for THz transparent materials. Based on these developments, THz imagers were fabricated and noise equivalent powers (NEPs) of THz-FPAs were measured at the wavelength range 3–270 μm. Finally, real-time THz images are presented, such as a reflection image, a transmission image through smoke, and a label-free detection image of the reaction of a small molecule with protein.

2. Previous works on real-time THz imaging

A.W.M. Lee et al. [4] described real-time THz imaging technology, using a commercially available uncooled infrared (IR) camera and quantum cascade laser (QCL). The uncooled IR camera employed 320×240 vanadium oxide (VOx) microbolometer infrared FPA (IRFPA) with 46.25 μm pixel pitch which had a sensitivity in the 8–14 μm long wavelength IR (LWIR) band. The germanium (Ge) lens for IR detection was replaced with an F/1 silicon (Si) meniscus lens to transmit THz radiation. The QCL radiated 4.3 THz line emission (70 μm in wavelength) with time-averaged power of 12.5 mW. The 4.3 THz line emission was focused on the IRFPA through a Ge vacuum package window and the THz signal was extracted, based on a method of cancellation of the common-mode LWIR signal. This method required three frames to obtain one frame of THz image, namely, 20 frames per second. The first frame contains both THz and LWIR signals, while no signals are extracted at the second frame which corresponds to the waiting time for THz signal to vanish and the third frame contains only LWIR signal. The LWIR signal extracted at the third frame is subtracted from the signals (THz + LWIR) extracted at the first frame and thus THz image can be obtained. The feasibility of a mail screening application was demonstrated by imaging the letters "MIT" written in pencil on the inside of a paper envelope. Noise equivalent power (NEP) of the IRFPA was found ~320 pW.

B.N. Behnken et al. [5] developed QCL and 2.8 THz (107 μm in wavelength) line emission from QCL was imaged with a commercially available uncooled LWIR camera which employed 160×120 pixel VOx microbolometer IRFPA. The pixels are made using a composite film of vanadium oxide (VOx) and silicon nitride (Si_3N_4) with 50 μm pixel pitch. The germanium lens for IR detection was replaced with a F/1 lens made of Picarin to transmit THz radiation. The QCL had time-averaged power of 0.4–1.4 mW. They showed a real-time THz image of a utility-knife blade wrapped in opaque plastic tape and increased image quality by using frame integration and MATLAB image-processing utility software.

N. Oda et al. [6] made NEP measurements on several uncooled VOx microbolometer IRFPAs, such as a 320×240 array with 37 μm pitch, a 320×240 array with 23.5 μm pitch, and a 640×480 array with 23.5 μm pitch, using uncooled LWIR cameras and QCL which radiated 3.1 THz line emission (97 μm in wavelength) with time-averaged power of 8.7 μW at the position of the IRFPA. The line emission from QCL was focused on the IRFPAs with off-axis parabolic mirrors, instead of using a Ge lens. The NEP values at 3.1 THz were found in a range of 200–300 pW, which is comparable to the NEP value obtained by A.W.M. Lee et al. [4].

3. Terahertz focal plane array (THz-FPA)

3.1. Thermal isolation structure of THz-FPA

The thermal detector, such as a bolometer, needs to be thermally isolated from the heat sink to increase sensitivity. A thermal isolation structure (TIS), i.e., a suspended microbridge structure, can satisfy this condition in that it prevents the heat collected by areas sensitive to THz radiation from escaping to the heat sink.

Fig. 1 shows schematic diagrams of the pixel structure of uncooled bolometer-type THz-FPA. The array format is 320×240 and pixel pitch is 23.5 μm. The pixel is divided into two parts, silicon (Si) readout integrated circuit (ROIC) in the lower part and suspended microbridge structure in the upper part. The Si-ROIC drives THz-FPA at TV frame rate.

The microbridge has a two-storied structure. The 1st floor is composed of a diaphragm and two legs, while the eaves structure is formed on the diaphragm to increase the sensitive area, or fill factor. The diaphragm and the eaves absorb THz radiation. The diaphragm is supported by the two legs so that the 1st floor is separated by air gap from Si-ROIC substrate and TIS is formed. The fabrication of TIS is carried out with surface micromachining technology [7].

The diaphragm is composed of bolometer thin film (vanadium oxide (VOx)), silicon nitride (SiNx) passivation layers and TiAlV electrodes, while the eaves structure is composed of SiNx layer and THz absorption layer (TiAlV thin metallic film). The leg is composed of electrically conductive thin film (TiAlV) and SiNx passivation layers. A reflection layer (Al) has been formed at the bottom of the air gap to provide an absorption mechanism for incident THz radiation.

THz absorption mechanism of TIS is explained as follows: In the wavelength region where the structural material used for the diaphragm and the eaves structure, namely, SiNx is transparent for THz radiation (beyond ca. 60 μm) [8], THz radiation first strikes the THz absorption layer and a part of radiation is reflected. The remaining radiation is transmitted and perfectly
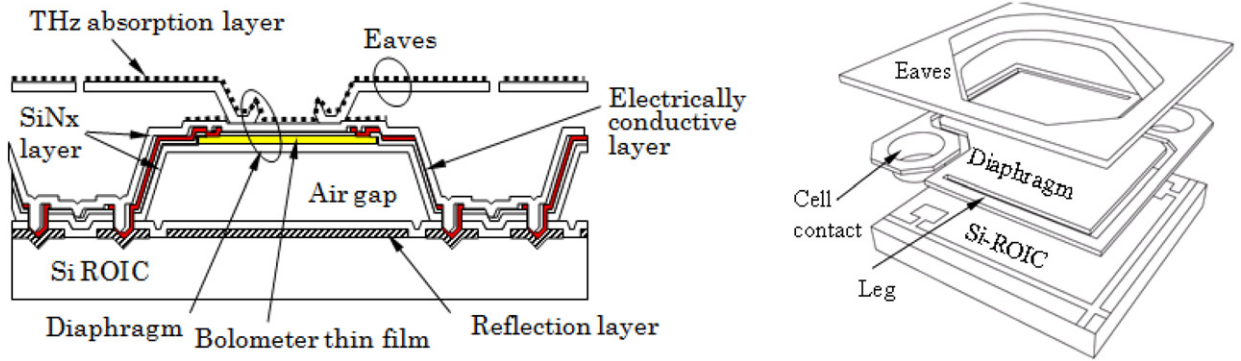
Fig. 1. Schematic diagrams of pixel structure of uncooled bolometer-type THz-FPA. (Left: cross sectional view; Right: oblique view.)
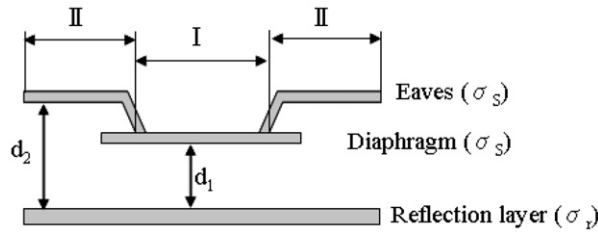

Fig. 2. Approximated thermal isolation structure.

reflected back to the THz absorption layer by the reflection layer. These two reflected radiations interfere destructively at the THz absorption layer and free carriers in the THz absorption layer absorb the THz radiation. The absorbed THz radiation heats the diaphragm and the eaves so that bolometer resistance changes. The resistance change of each pixel is converted to voltage change by supplying each pixel with a bias current. Each voltage change is read out to form THz image at TV frame rate. On the other hand, in wavelength region where the structural material, i.e., SiNx, is not transparent for THz radiation (below ca. 50 μm) [8], incident THz radiation is partly absorbed by SiNx and the remaining radiation is transmitted and perfectly reflected back to the diaphragm and the eaves by the reflection layer. Consequently, the incident THz radiation doubly passes the diaphragm and the eaves and is absorbed by them which are then heated up and bolometer resistance changes.

3.2. Calculations of absorptance for thermal isolation structure

Responsivity (R_V) of microbolometer which has thermal isolation structure (TIS) is expressed by following formula:

$$R_V = \frac{\alpha \eta V_B}{G} \quad \text{[V/W]} \tag{1}$$

Here, α is temperature coefficient of resistance (TCR) of bolometer material, η is total absorptance of diaphragm and eaves, G is thermal conductance of leg and V_B is bias voltage applied to bolometer. In the case of our IRFPA, values of TCR, η, G and V_B are ca. -1.5%/K at 40 °C, 80% at LWIR, 30 nW/K and 4 V, respectively. An approximated thermal isolation structure is shown in Fig. 2 and its total absorptance (η) is approximated by a linear combination of diaphragm absorptance $A(\lambda, d_1)$ and eaves absorptance $A(\lambda, d_2)$ as follows [9]:

$$A(\lambda, d_1) = \frac{4}{Dn^2} \left\{ \left[f_s (f_r + 1)^2 / n^2 + f_r \right] \sin^2 \theta + (f_r + f_s) \cos^2 \theta \right\} \tag{2}$$

where

$$D = \left[(f_r + 1)(f_s + 1)/n^2 + 1 \right]^2 \sin^2 \theta + \left[(f_r + f_s + 2)^2 / n^2 \right] \cos^2 \theta$$

$$f_r = 120\pi / \sigma_r$$

$$f_s = 120\pi / \sigma_s$$

$$\theta = 2\pi n d_1 / \lambda$$

$$\eta = \beta_1 A(\lambda, d_1) + \beta_2 A(\lambda, d_2) \tag{3}$$

Table 1
Summary of parameters for the diaphragm and eaves.

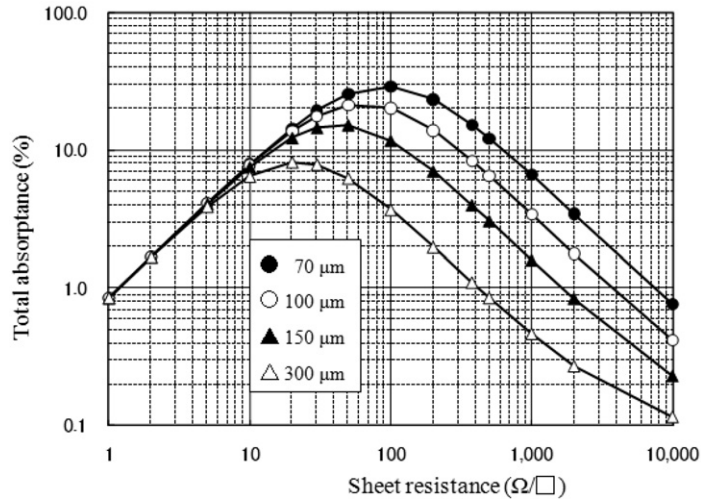| Zones	Air gap	Areal occupancy ratios
Diaphragm (zone 1)	$d_1 = 1.5$ μm	$\beta_1 = 20\%$
Eaves (zone 2)	$d_2 = 3.0$ μm	$\beta_2 = 60\%$

Fig. 3. Relation of total absorptance of TIS to sheet resistance of the THz absorption layer at several wavelengths (70, 100, 150, 300 μm).
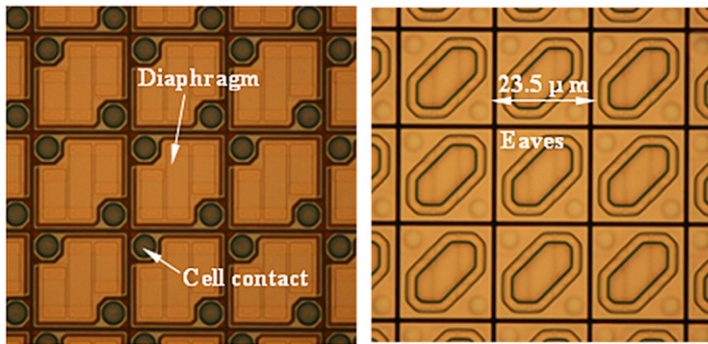

Fig. 4. Micrographs of a part of uncooled bolometer-type 320 × 240 THz-FPA with pixel pitch of 23.5 μm. (Left: the first floor; Right: the second floor.)

Here, λ is a wavelength, n is a refractive index of air gap ($n = 1$), d_1 and d_2 are air gaps (see Fig. 2), σ_r is a sheet resistance of reflection layer and σ_s is a sheet resistance of THz absorption layer or thin metallic film, while β_1 and β_2 are areal occupancy ratios for the diaphragm and eaves of the pixel, respectively. Table 1 summarizes parameters for diaphragm and eaves of pixel. The fill factor of the eaves (ca. 90%) is not used in the table because there is no reflection layer at two cell contacts (see Fig. 1). Using these formulae and parameters, one can obtain relation of total absorptance of TIS to sheet resistance of the THz absorption layer at several wavelengths (70, 100, 150, 300 μm), which is shown in Fig. 3.

3.3. Fabrication of uncooled bolometer-type 320 × 240 THz-FPAs

It can be seen in Fig. 3 that the optimum sheet resistance of the THz absorption layer is in a range of 20–200 Ω/square for detection of 3 THz radiation (100 μm in wavelength). So, THz-FPAs have been fabricated with sheet resistances aimed at 20, 40 and 100 Ω/square for the THz absorption layer (TiAlV metallic thin film). Fabrication process of THz-FPA is based on that of IRFPA with pixel pitch of 23.5 μm [7] and modification for THz detection is an addition of process of forming THz absorption layers on both diaphragm and eaves. Micrographs of THz-FPA thus fabricated are shown in Fig. 4 and the sheet resistances of the THz absorption layers were measured as 21, 44 and 134 Ω/square.
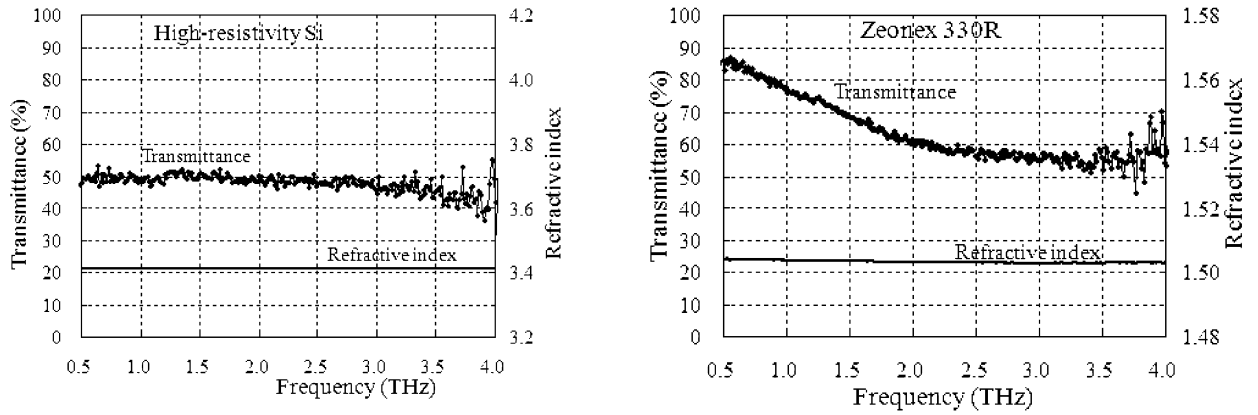
Fig. 5. Transmittances and refractive indices of two materials in THz region. (Left: *n*-type high resistivity Si disk (5.02 mm thick, 19–20 kΩ cm); Right: Zeonex 330R disk (5.03 mm thick).)
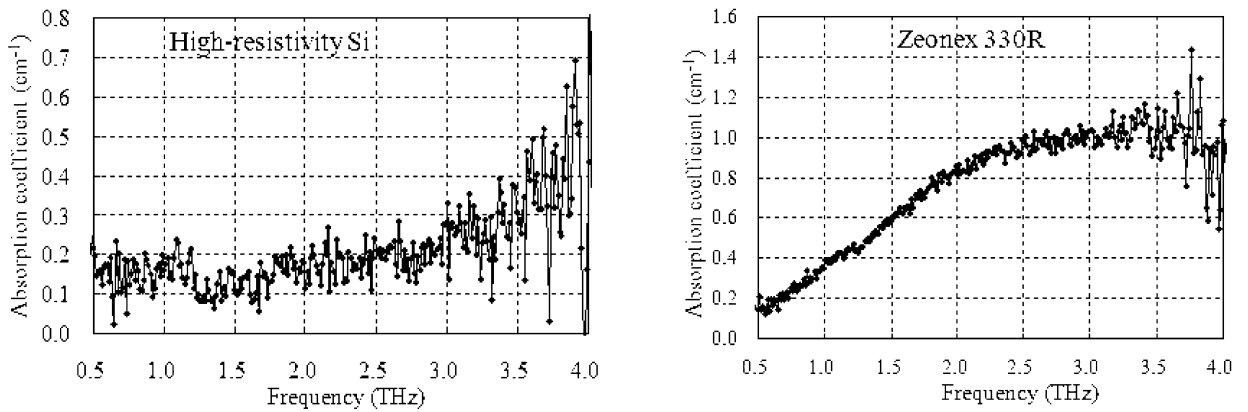

Fig. 6. Characteristics of absorption coefficients for high resistivity Si (left) and Zeonex 330R (right).

4. THz transparent material for lens and window

4.1. Search for THz transparent material

Spectral characteristics in THz region have been measured for a number of materials, such as semiconductors, polymers and so forth. Among them, high-resistivity silicon (HR-Si) [10] and cyclic olefin copolymers (COC) are candidates for THz transparent materials which can be applied to lens and window. Fig. 5 shows transmittances and refractive indices in frequency range of 0.5–4.0 THz for *n*-type HR-Si with resistivity of 19–20 kΩ cm and Zeonex 330R (COC). Thicknesses of these materials are ca. 5 mm. The transmittance of HR-Si is very flat, around 50%, while that of Zeonex 330R decreases with frequency increase.

One of important parameters for fabricating lens and window is absorption coefficient of material. An absorption coefficient (α) is calculated, using transmittance and following formula [11]:

$$T = \frac{(1-R)^2 e^{-\alpha d}}{1 - R^2 e^{-2\alpha d}}$$

$$R = \frac{(1-n)^2}{(1+n)^2} \tag{4}$$

Here, T is transmittance, d is sample thickness, R is single-surface reflectance and n is refractive index. Using data shown in Fig. 5, absorption coefficients are obtained for HR-Si and Zeonex 330R (see Fig. 6). Fig. 6 shows that the absorption coefficient of HR-Si is much smaller than that of Zeonex 330R. It is concluded that HR-Si is much better candidate for THz transparent material to fabricate lens and window for THz camera. Large value of refractive index of HR-Si facilitates lens design for THz optics, while the large refractive index induces large reflection loss. Therefore, an anti-reflection coating film has to be formed on both sides of HR-Si to increase transmittance from ca. 50% to more than 90%.
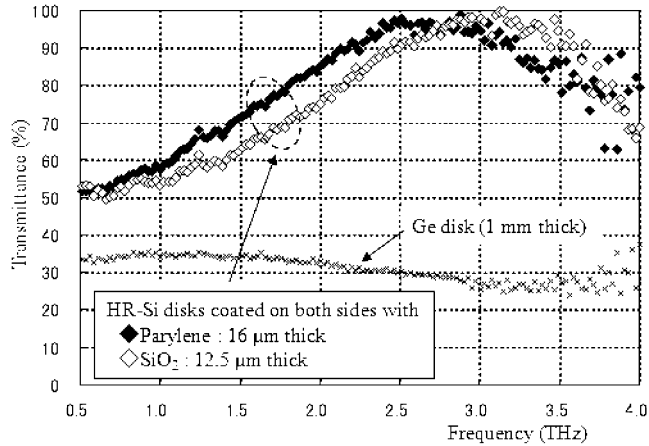
Fig. 7. Transmittance curves for HR-Si disks (1 mm thick) coated on both sides with 16 µm-thick Parylene C film and 12.5 µm-thick SiO$_2$ film. Transmittance curve of 1 mm-thick Ge disk is also shown for comparison.
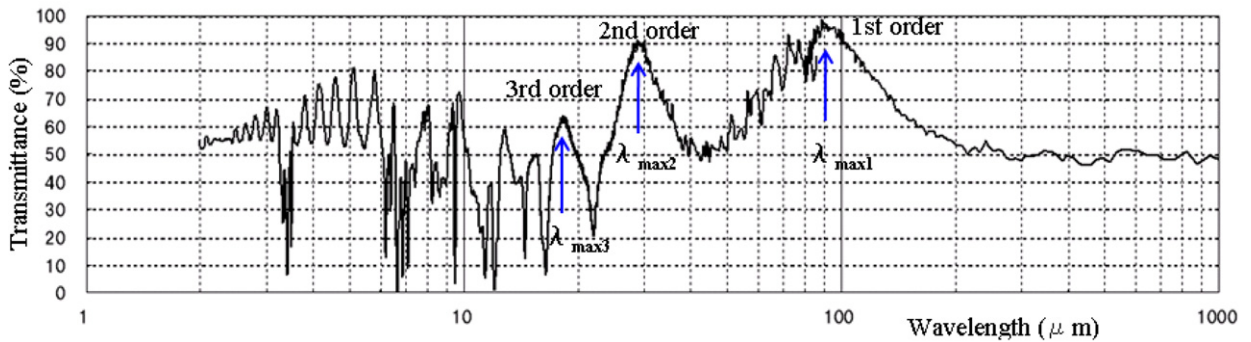

Fig. 8. Transmittance curve of 1 mm-thick HR-Si disk coated on both sides with 12.5 µm-thick Parylene C film.

4.2. Anti-reflection coatings for THz transparent material

Refractive index of anti-reflection coating (ARC) film for HR-Si should be ca. 1.8. Two kinds of ARC films, parylene C film [12] and SiO$_2$ film, were formed on both sides of HR-Si substrates. Fig. 7 shows transmittance curves of 1 mm-thick HR-Si disks coated on both sides with 16 µm-thick parylene C film and 12.5 µm-thick SiO$_2$ film as well as transmittance curve of 1 mm-thick Ge disk which is transparent for LWIR. It can be seen in the figure that transmittance is improved by a factor of 3–4 as compared with Ge disk. Transmission curve of 1 mm-thick HR-Si disk coated on both sides with 12.5 µm-thick Parylene C film was measured in wavelength range of 2 µm to 1 mm (see Fig. 8). One can find a couple of peaks at λ_{max1}, λ_{max2} and λ_{max3} which correspond to first order, second order and third order interferences. Fig. 9 shows relation of λ_{max1} to parylene thickness.

5. THz imagers

Two situations are considered for short range standoff imaging, such as about 1 m square field of view (FOV) at 5 m distance and about 10 cm square FOV at 5 m distance with the same spatial resolution of about 1 cm. Table 2 summarizes parameters for two THz imagers (handy THz camera and THz telescope) to achieve these two imaging situations.

The THz imagers are shown in Fig. 10(a) which is composed of handy THz camera and THz telescope. The handy THz camera has thin lens optics with F/1 and focal length of 28 mm, using Parylene anti-reflection (AR) coated HR-Si. As is shown in Fig. 10(b), the optics is composed of two thin lenses, namely, non-spherical lens and Fresnel lens. The surface shape of the non-spherical lens is approximated by sixth-order polynomial and the number of grooves of the Fresnel lens is fifteen (see Fig. 10(c)). Maximum thickness of the optics is 3 mm in total and thickness of Parylene AR-coating for the optics is fitted to ca. 40 µm in wavelength where optics has peak transmittance (see Fig. 9). The vacuum package (see Fig. 10(d)) which contains THz-FPA is incorporated in the handy THz camera and the material of the package window is Parylene AR-coated HR-Si disk which also has peak transmittance at ca. 40 µm. The THz telescope has non-spherical mirror with F/1
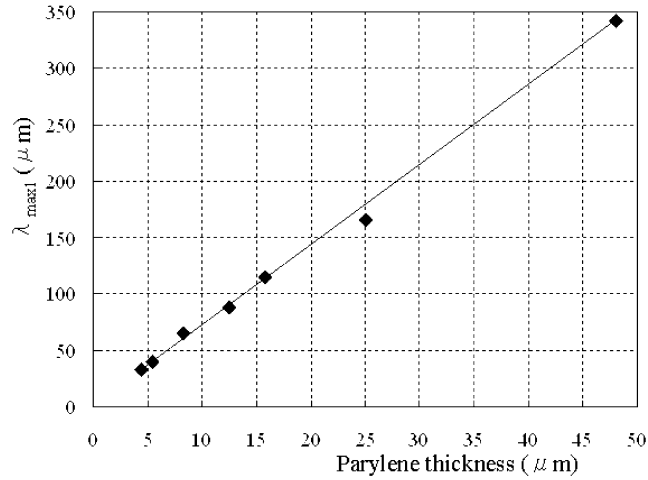
Fig. 9. Relation of $\lambda_{\max 1}$ to parylene thickness.

Table 2
Parameters for two THz imagers.

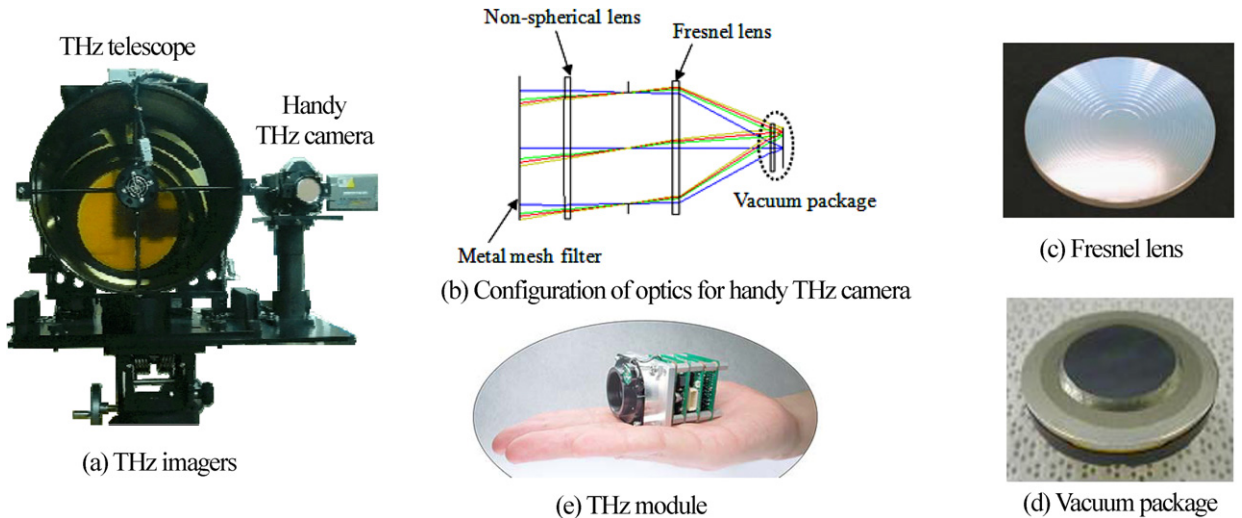|	Handy THz camera	THz telescope
THz-FPA	320 × 240, 23.5 μm pixel pitch	
FOV	15.5° × 11.5° (1.3 × 1 m at 5 m)	1.55° × 1.15° (13 × 10 cm at 5 m)
Focal length: F number	28.2 mm: F/1	282 mm: F/1
IFOV (Instantaneous FOV)	0.83 mrad (0.42 cm at 5 m)	83 μrad (0.042 cm at 5 m)
Spatial resolution	2 mrad (1 cm square)	
Fraunhofer diffraction limit	1.7 mrad at 40 μm	0.38 mrad at 90 μm
The number of pixels which correspond to spatial resolution	2.4 × 2.4 pixels	24 × 24 pixels

Fig. 10. (a) THz imagers composed of handy THz camera and THz telescope, (b) Configuration of optics for handy THz camera, (c) Thin Fresnel lens (1.5 mm thick, 32 mm in diameter), (d) Vacuum package, (e) THz module.

and focal length of 282 mm, whose surface is approximated by sixth-order polynomial. Small THz module (see Fig. 10(e)) is placed at main focus of the mirror and it contains another vacuum package whose window has peak transmittance at ca. 100 μm to efficiently detect line emission at 3 THz from QCL.

Table 3
Experimental equipment used for NEP measurements at several wavelengths.

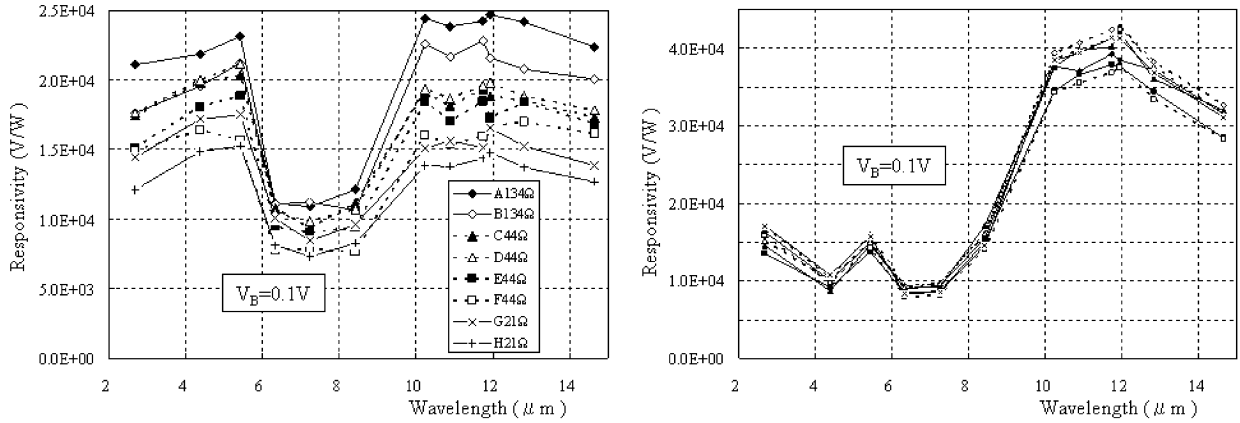| Wavelength	Radiation source	Filter
3–14 μm	Blackbody (1173 K)	Twelve narrow band pass filters
31–43 μm		Long pass MMF ($\lambda \geqslant 30$ μm)
55–95 μm		Long pass MMF ($\lambda \geqslant 56$ μm)
72–107 μm		Band pass MMF (72–107 μm)
97 μm (3.1 THz)	Quantum cascade laser	Band pass MMF (72–107 μm)
273 μm (1.1 THz)	Backward wave oscillator	Long pass MMF ($\lambda \geqslant 56$ μm)

Fig. 11. Wavelength dependences of responsivities for TEG devices. (Left: TEG for THz-FPA; Right: TEG for IRFPA.)

6. Measurements of sensitivity

Measurements of NEP (noise equivalent power) and responsivity were carried out at several wavelengths with handy THz camera. Table 3 summarizes experimental conditions for NEP measurements. Radiation sources, such as blackbody, quantum cascade laser (QCL) and backward wave oscillator (BWO), were used. In the case of usage of QCL and BWO, metal mesh filters (MMFs) were put between radiation source and THz camera to block infrared radiation. Combinations of blackbody with MMFs were taken for the measurements in wavelength range from infrared to ca. 100 μm, since monochromatic wave sources were not easily obtained in this wavelength range. In this case, shorter and longer wavelengths which give half maximum of $\tau(\lambda)B(\lambda, T)$ curve are calculated, where $\tau(\lambda)$ is overall transmission curve of MMF and lens, $B(\lambda, T)$ is Planck function and T is absolute temperature.

Fig. 11 shows the measured responsivities in wavelength range of 3–14 μm. The left figure shows responsivities of THz-FPAs with three different sheet resistances for THz absorption layer (21, 44, 134 Ω/square), while the right figure shows those of IRFPA. Device used for measurements is single element located around FPA, so-called TEG (Test Element Group) and the TEG has the same structure as the pixel of FPA has. It can be seen that the TEG devices with 134 Ω/square have higher responsivity than devices with lower sheet resistances have. Low DC bias voltage of 0.1 V was applied to TEG during responsivity-measurements to avoid damage of the TEG due to Joule heat. Since pulsed bias voltage of 4 V was applied to both THz-FPA and IRFPA under drive conditions of both FPAs, the responsivities shown in Fig. 11 are multiplied by a factor of 40 in accordance with the formula (1). The multiplied responsivity corresponds to NEP value of ca. 10 pW for IRFPA (right figure) at 8–14 μm wavelength band [6], which provides these THz-FPAs with NEP values for 3–5 μm and 8–14 μm bands (see Table 4 and Fig. 14). Here, it should be mentioned that since major noise components of bolometer-type FPA are $1/f$ noise, Johnson noise and circuit noise, the total noise of the FPA is independent of wavelength and it is calculated to be ca. 16 μV. It turns out that NEP values of THz-FPA at 3–5 μm are improved (by a factor of two for sheet resistance of 134 Ω/square), while NEP values of THz-FPA at 8–14 μm is degraded. The error bars of NEP in 3–5 and 8–14 μm bands cover NEP values of devices with three different sheet resistances (see Table 4 and Fig. 14).

The spectral responsivity curves shown in Fig. 11 are explained in accordance with the previous Section 3.1 as follows: Honeywell's patent [13] shows that passivation layer of SiNx absorbs radiation of 8–14 μm wavelength (LWIR), while SiNx hardly absorbs radiation of 3–5 μm wavelength (MWIR). In the absence of the THz absorption layer (IRFPA case), SiNx passivation layer simply absorbs LWIR absorption. On the other hand, in the presence of THz absorption layer (THz-FPA case), LWIR radiation is slightly reflected by the THz absorption layer (thin metallic film) and LWIR responsivity is degraded, while optical interference occurs at MWIR between the THz absorption layer and reflection layer (see Fig. 1) and MWIR responsivity is enhanced.

As to NEP measurements in 31–43, 55–95 and 72–107 μm wavelength bands, images of a blackbody were taken at 60 Hz, using handy THz camera equipped with metal mesh filter (MMF) in front of lens optics. The intensity profiles of the
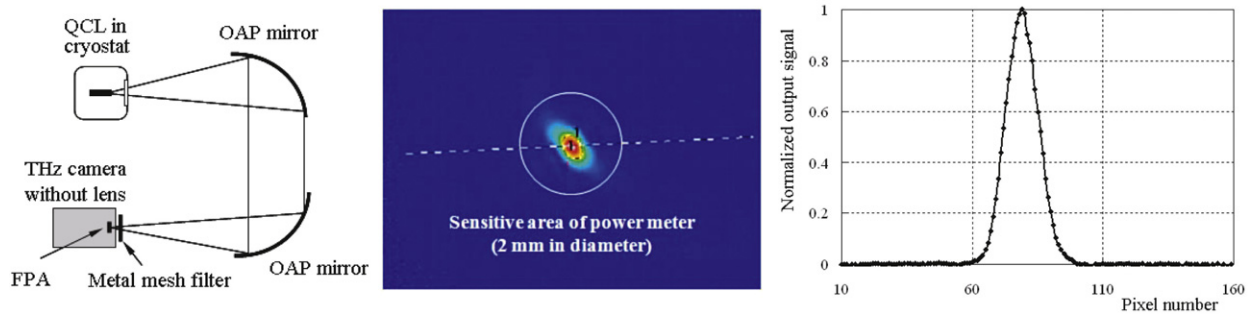
Fig. 12. Left: Experimental setup for NEP measurements. Center: Real-time THz image of line emission from QCL at 3.1 THz. Right: Normalized intensity profile along dashed line in the central figure.
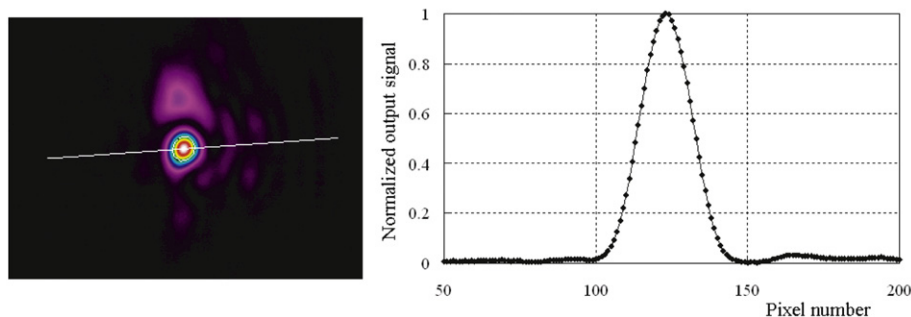

Fig. 13. Left: Real-time THz image of line emission from BWO at 1.1 THz. Right: Normalized intensity profile along the line in the left figure.

images were used to calculate signal-to-noise ratios and NEP values. The NEP values thus obtained have some ambiguity probably due to influence of multiple reflection inside multi-layers of MMF and/or between MMF and blackbody source. The ambiguity is expressed by error bars (see Table 4 and Fig. 14).

Real-time images of THz radiation from QCL (3.1 THz, 97 μm) were obtained at 60 Hz with 320×240 THz-FPA (pixel pitch of 23.5 μm). The left figure of Fig. 12 shows experimental setup for NEP measurements. The divergent beam from QCL was collimated with first off-axis parabolic (OAP) mirror and was focused on THz-FPA by second OAP mirror. In this setup, THz lens optics was removed from the handy THz camera. Metal mesh filter (MMF) was put in front of THz-FPA to block LWIR and transmit 3.1 THz radiation. Central and right figures of Fig. 12 show real-time THz image of line emission from QCL at 3.1 THz and normalized intensity profile along dashed line. The FPA was driven at frame rate of 60 Hz. The circle shown in the central figure corresponds to sensitive area of power meter (2 mm in diameter), with which time-averaged THz power from QCL was measured to be 16 μW. Using these experimental data, noise equivalent power (NEP) at 3.1 THz can be estimated for eight THz-FPAs with 23.5 μm pixel pitch. The area of QCL image is approximated by half-maximum contour which contains ca. 240 pixels. Considering signal-to-noise ratio of intensity profile and transmission values of both metal mesh filter and vacuum package window, NEP values for eight THz-FPAs are estimated to be 41 ± 4 pW at 3.1 THz. There seems no obvious correlation between NEP and sheet resistance. This NEP value is converted to total absorptance of ca. 20% which is consistent with the calculations (see Fig. 3).

NEP measurements at 1.1 THz (273 μm in wavelength) were made with backward wave oscillator (BWO) in a similar way to those made with QCL. Four OAP mirrors were used instead of lens optics of the handy THz camera. Fig. 13 shows real-time image of line emission from BWO and normalized intensity profile. The NEP value at 273 μm is calculated in the same way as the case for QCL. Since power meter is hardly available at this wavelength region, nominal output power (5 mW) listed in BWO catalog is used for the calculation of NEP. Furthermore, atmospheric transmission at 273 μm is estimated to be ca. 60%, based on measured value of absorption coefficient of atmosphere and distance between BWO and THz-FPA (ca. 80 cm). The NEP value thus obtained is considered as an upper limit.

The NEP values thus measured are summarized in Table 4 and Fig. 14. The table contains two NEP values (units of W and $W\,Hz^{-1/2}$) for each measurement. The bandwidth of the electronics (42.7 kHz) for the handy THz camera is used for conversion from W to $W\,Hz^{-1/2}$. It can be seen in the figure that wavelength dependence of NEP is quite flat below 100 μm for THz-FPA thus developed.

Effects of frame integration and pixel integration on NEP values were investigated. Fig. 15 shows the relation of improvement in signal-to-noise ratio (SNR) to the number of frame integration. The improvement factor is only in a range of 2–3, because $1/f$ noise is dominant for THz-FPAs. Pixel integration of 3×3 and 24×24 were taken (see Table 2), taking into account IFOV and spatial resolution. In the experiments, THz images of radiation from QCL were defocused and enlarged over area more than 24×24 pixels and frame rate of about 1 Hz was taken, namely, 64 frame integration. The THz images

Table 4
Summary of NEP measurements.

| Wavelength	Sheet resistance of THz absorption layer		
	134 Ω/square	44 Ω/square	21 Ω/square
3–5 μm	17 pW, 8.5×10^{-14} W Hz$^{-1/2}$	21 pW, 1.1×10^{-13} W Hz$^{-1/2}$	23 pW, 1.2×10^{-13} W Hz$^{-1/2}$
8–14 μm	16 pW, 8.0×10^{-14} W Hz$^{-1/2}$	21 pW, 1.1×10^{-13} W Hz$^{-1/2}$	26 pW, 1.3×10^{-13} W Hz$^{-1/2}$
31–43 μm	32–41 pW $(1.6–2.1) \times 10^{-13}$ W Hz$^{-1/2}$	–	–
55–95 μm	–	25–43 pW, $(1.3–2.2) \times 10^{-13}$ W Hz$^{-1/2}$	–
72–107 μm	–	30–75 pW, $(1.5–3.8) \times 10^{-13}$ W Hz$^{-1/2}$	–
97 μm (3.1 THz)	41 ± 4 pW, $(2.1 \pm 0.2) \times 10^{-13}$ W Hz$^{-1/2}$	41 ± 4 pW, $(2.1 \pm 0.2) \times 10^{-13}$ W Hz$^{-1/2}$	41 ± 4 pW, $(2.1 \pm 0.2) \times 10^{-13}$ W Hz$^{-1/2}$
273 μm (1.1 THz)	–	<2 nW, $< 1 \times 10^{-11}$ W Hz$^{-1/2}$	–
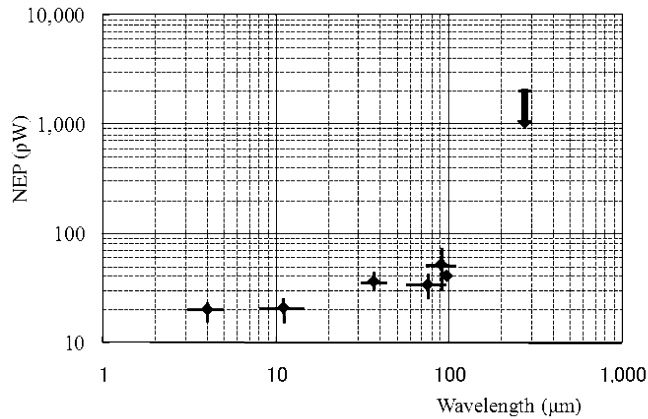
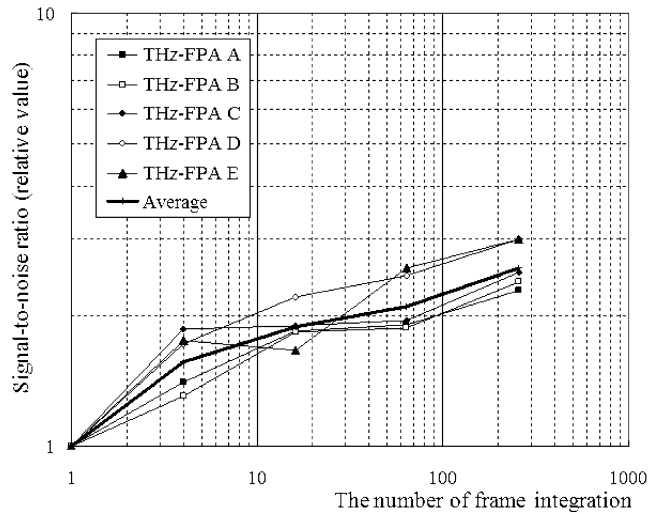**Fig. 14.** Summary of wavelength dependence of NEP for THz-FPAs.

Fig. 15. Relation of improvement in signal-to-noise ratio to the number of frame integration.

thus obtained are shown in Fig. 16(a), (b) and (c), along with normalized intensity profiles. Fig. 16(a) is just defocused image at 60 Hz frame rate without pixel integration, where NEP value is 41 pW. The pixel integration of 3×3 further improved NEP value by a factor of 8, namely, 5 pW and hardly changed details of image (Fig. 16(b)), while the pixel integration of 24×24 further improved NEP value by a factor of 60, namely, 0.7 pW and smeared out the details of image (Fig. 16(c)). These experiments show that signal processing can further improve NEP value by another factor.
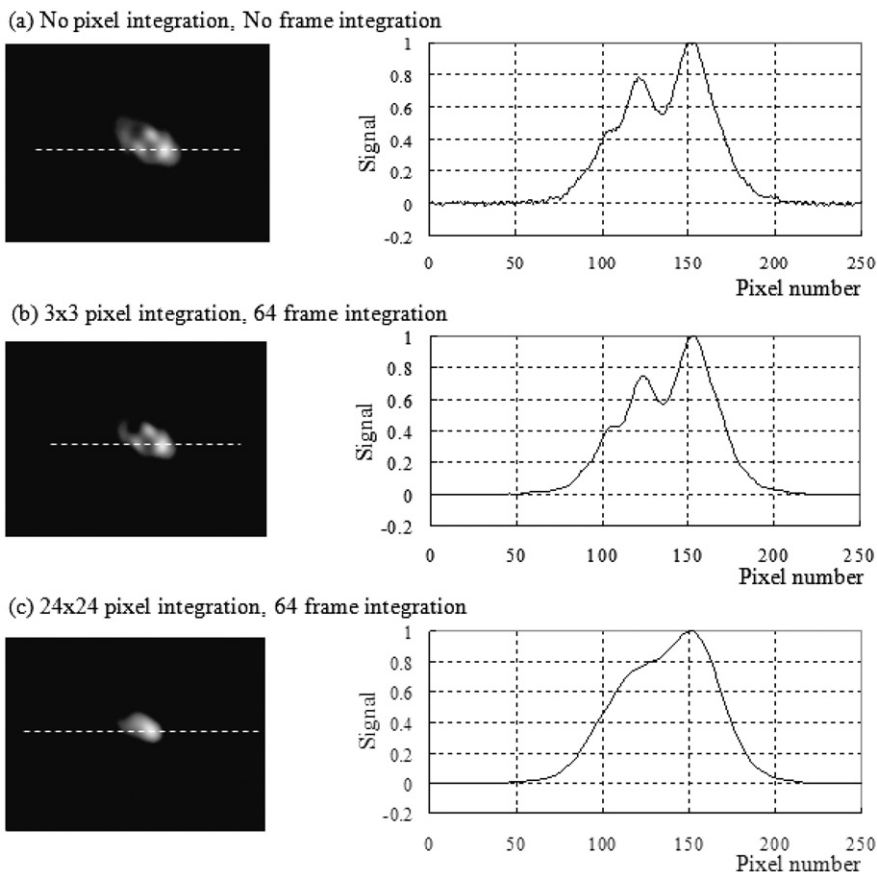
Fig. 16. Effect of pixel integration. Defocused images and normalized intensity profiles along dashed lines. (a) No pixel integration, no frame integration, (b) 3 × 3 pixel integration, 64 frame integration, (c) 24 × 24 pixel integration, 64 frame integration.
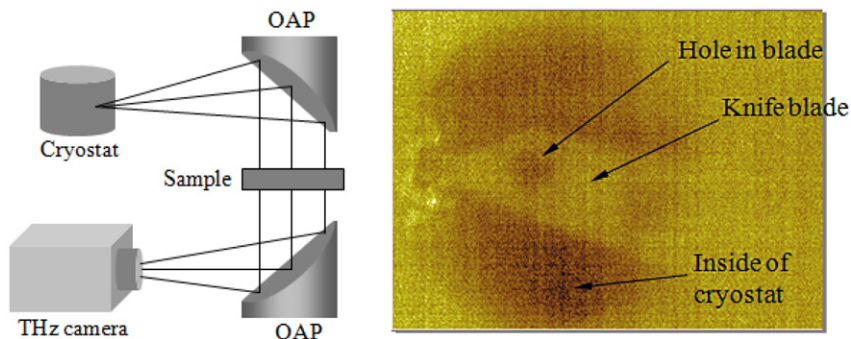

Fig. 17. Left: Experiment setup; Right: Real-time THz transmission image of knife blade put in black polyethylene bag (single frame, no pixel integration).

7. Real-time THz imageries

Fig. 17 shows the experimental setup for passive THz imaging and the real-time THz transmission image of knife blade put in black polyethylene (PE) bag. A long pass metal mesh filter with cut-on wavelength of 30 μm was incorporated in the handy THz camera. Thermal radiation from the blade (room temperature) is detected through the black PE bag with background radiation from inside of cryostat (15 K).

Fig. 18 shows the experiment setup and the real-time THz reflection image of coin. The line emission of 3.1 THz from a quantum cascade laser (QCL) was collimated with an off-axis parabolic (OAP) mirror and was irradiated on the Chinese coin (1 Yuan). The time-averaged power of QCL was 7 μW. The reflection image of the coin was taken, using the handy THz camera with long-pass metal mesh filter of 30 μm cut-on wavelength. A feature corresponding to visible picture can be seen in the real-time reflection image.
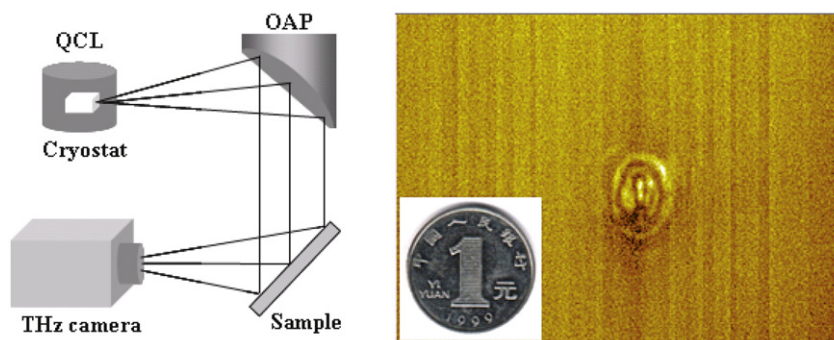
Fig. 18. Left: Experiment setup; Right: Real-time THz reflection image of coin (single frame, no pixel integration).
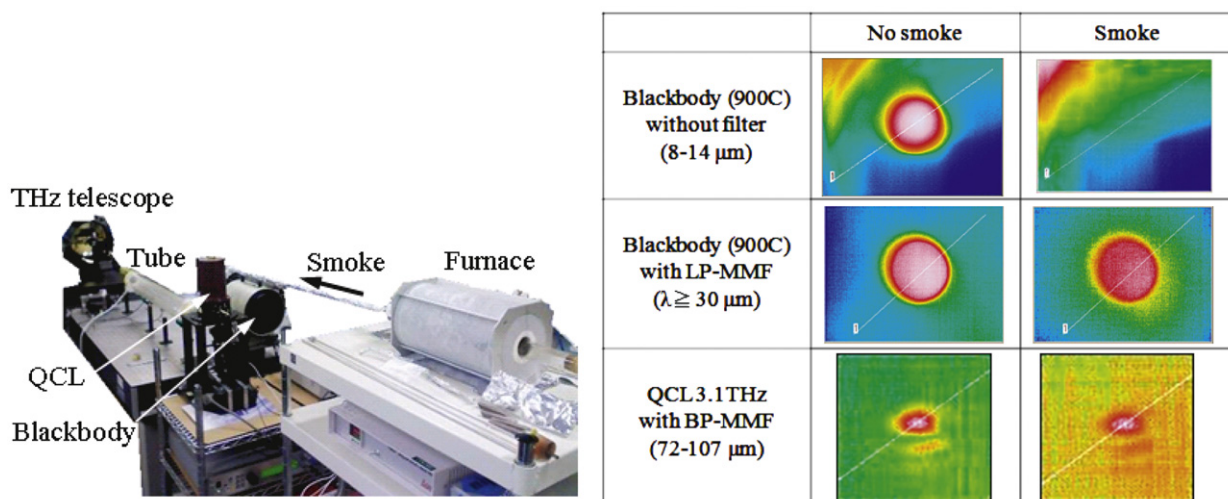

Fig. 19. Left: Experimental setup; Right: Imageries without and with smoke (single frame, no pixel integration).

Fig. 19 shows the experiment setup and images of radiation sources (blackbody, QCL) through smoke, taken at 8–14 μm (LWIR) and the THz region. Smoke was generated by burning tips of cherry-blossom at 450 °C in a furnace and introduced into the tube which was then put between the THz telescope and radiation sources (blackbody, QCL). Metal mesh filter (MMF) was incorporated into the THz telescope. Two kinds of MMF were used. One was a long-pass MMF (LP-MMF) with 30 μm cut-on wavelength and other was a band-pass MMF (BP-MMF) with wavelength range of 72–107 μm. When MMF was not incorporated, the telescope mainly detected LWIR radiation. Fig. 19 (right) shows images without smoke and with smoke. In the absence of smoke, the radiation sources (blackbody, QCL) were observed at both LWIR and THz regions. In the presence of smoke, the radiation source was not observed at LWIR, while the radiation sources were observed in THz region. This is because scattering extinction coefficient at THz is much smaller than that at LWIR.

Fig. 20 shows a real-time transmission image which is the label-free detection image for reaction of small molecule (Biotin, molecular weight: 244) with protein (Streptavidin, molecular weight: ca. 60,000). This sample was fabricated such that Biotin (Vitamin B) was immobilized on a PVDF (Polyvinylidene difluoride) membrane with PEG (polyethyleneglycol) and MPEG (methyl ether PEG) as linkers and the membrane thus prepared was exposed to a reagent of Streptavidin dissolved in ethanol which was deposited on the membrane-like spot array. The amount of reagent was 0.1 μL for each spot and the molar concentration (mol/L) of Streptavidin was controlled in a range of 1×10^{-2} to 8×10^{-5}. The molar concentration of 8×10^{-5} contains Streptavidin of 0.5 μg/spot.

The sample was put between high-pressure Hg lamp (THz radiation source) and handy THz camera with long-pass MMF of 30 μm cut-on wavelength. The gray area of the upper figure was chosen as real-time imaging area. Three real-time images were taken because the THz radiation source was too small to cover the gray area at the same time. There was non-uniformity in brightness of the radiation source. Spots with molar concentration from 1×10^{-2} to 8×10^{-5} are recognized as absorption spots, although signal-to-noise ratios are small. The real-time images for the same sample were also taken with LWIR camera (wavelength range of 8–14 μm), but spots were not observed. These imaging experiments indicate that real-time THz imaging technology is very promising to realize label-free detection of antigen–antibody reaction and exploration of ligand, which may open new paradigm for various fields, such as life science, medicals, pharmaceuticals and so on.
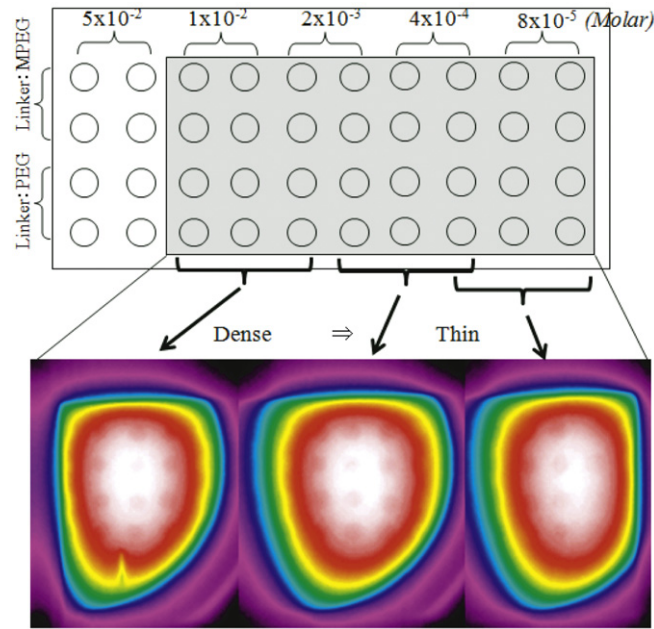
Fig. 20. Label-free detection images (single frame, no pixel integration) for reaction of small molecule (Biotin) with protein (Streptavidin).
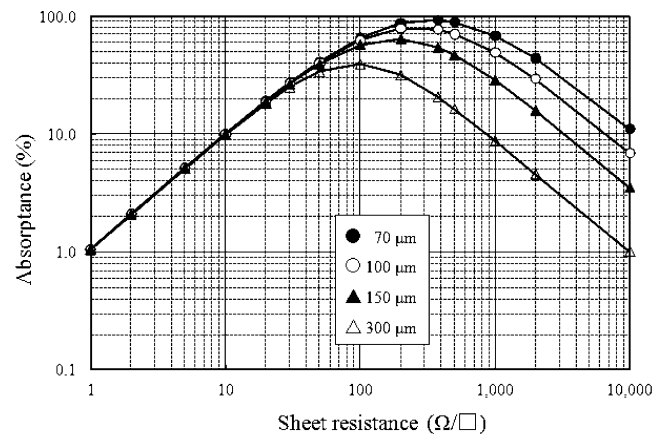

Fig. 21. Relation of absorptance of TIS to sheet resistance of THz absorption layer for air gap of 12 μm at several wavelengths (70, 100, 150, 300 μm).

8. Summary

This article describes state-of-the-art on uncooled bolometer-type THz focal plane arrays and THz transparent materials for lens and package window. A handy THz camera and THz telescope were fabricated, based on these technologies. The NEP measurements show that THz-FPAs thus developed have nearly flat spectral response below 100 μm in wavelength. Signal integrations were also carried out and improvement in NEP by a factor of 8 was obtained (ca. 5 pW) for the handy THz camera. Real-time THz imageries were obtained at 60 Hz frame rate with the handy THz camera and the THz telescope. One of the images indicates that THz technology is promising for label-free detection of reaction of small molecules with proteins.

It is finally mentioned that an uncooled bolometer-type THz-FPA still has a room for improvement in NEP. Fig. 21 shows the relation of absorptance of thermal isolation structure (TIS) to sheet resistance of THz absorption layer for air gap of 12 μm at several wavelengths (70, 100, 150, 300 μm). Comparing this figure with Fig. 3, it is predicted that absorptance, accordingly, NEP can be improved by another factor of 3–10. Thus, uncooled bolometer-type THz-FPA is very promising for real-time THz imaging.

Acknowledgements

References

[1] K. Kawase, Terahertz imaging for drug detection and large-scale integrated circuit inspection, Optics & Photonics News 15 (2004) 34–39.
[2] Y. Chen, et al., THz spectra of 4-NT and 2, 6-DNT, Proc. SPIE 6212 (2006) 62120P-1–62120P-7.
[3] T. Globus, et al., THz resonance spectra of bacillus subtilis cells and spores in PE pellets and dilute water solutions, Proc. SPIE 6212 (2006) 62120K-1–62120K-12.
[4] A.W.M. Lee, et al., Real-time imaging using a 4.3-THz quantum cascade laser and a 320×240 microbolometer focal-plane array, IEEE Photonics Technology Letters 18 (2006) 1415–1417.
[5] B.N. Behnken, et al., Real-time imaging using a 2.8 THz quantum cascade laser and uncooled infrared microbolometer camera, Optics Letters 33 (2008) 440–442.
[6] N. Oda, et al., Detection of Terahertz radiation from quantum cascade laser, using vanadium oxide microbolometer focal plane arrays, Proc. SPIE 6940 (2008) 69402Y-1–69402Y-12.
[7] S. Tohyama, et al., New thermally isolated pixel structure for high-resolution (640×480) uncooled infrared focal plane arrays, Optical Engineering 45 (014001) (2006) 014001-1–014001-10.
[8] Q. Hu, et al., Real-time THz imaging using quantum-cascade lasers and focal-plane array cameras, in: 2nd International Workshop on Quantum Cascade Lasers, Brindisi, Italy, September 6–9, 2006.
[9] P.A. Silberg, Infrared absorption of three-layer films, J. Opt. Soc. Am. 47 (1957) 575–578.
[10] Jianming Dai, et al., Terahertz time-domain spectroscopy characterization of the far-infrared absorption and index of refraction of high-resistivity, float-zone silicon, J. Opt. Soc. Am. B 21 (2004) 1379–1386.
[11] D.C. Harris, Materials for Infrared Windows and Domes: Properties and Performance, in: Monograph, vol. PM70, SPIE Press, Bellingham, Washington, 1999, p. 24.
[12] A.J. Gatesman, et al., An anti-reflection coating for silicon optics at Terahertz frequencies, IEEE Microwave and Guided Wave Letters 10 (2000) 264–266.
[13] B.E. Cole, Microstructure design for high IR sensitivity, United State Patent 5286976, 1994.